Supporting Information for Sign of Mechanochemical Curvature Governing O_2 Activation Mechanisms and Reactivity on Rippled Supports

Sayan Banerjee*

Department of Chemistry, University of Tennessee, Knoxville, Knoxville, TN 37923, USA

Table of Contents

1. Computational Details and Benchmarking

Density functional theory (DFT) calculations were performed using the Quantum Espresso software package.[1] The generalized gradient approximation (GGA) with the Perdew–Burke–Ernzerhof (PBE) exchange–correlation functional was employed.[2] Ultrasoft GBRV pseudopotentials were used with kinetic-energy and charge-density cutoffs of 35 Ry and 350 Ry, respectively.[3] Dispersion interactions were included via the DFT-D3 correction developed by Grimme and co-workers.[4] A (6 × 6) graphene supercell was used to investigate curvature effects on adsorption, with a vacuum spacing of approximately 20 Å along the surface normal. A Γ-centered (2 × 2 × 1) Monkhorst–Pack grid was used to sample the Brillouin zone.[5] All structures were fully relaxed until the forces on each atom were below 1.0×10^{-3} a.u., and the total-energy convergence criterion was set to 1.0×10^{-4} a.u.

To ensure thermodynamic consistency of the four-electron oxygen reduction reaction (ORR) cycle, we verified that the sum of the calculated free-energy changes for the four proton–electron transfer steps, $\sum_i \Delta G_i$, must equal $-4eU_{\mathrm{eq}} = -4.92$ eV at equilibrium. Our DFT-based values yielded $\sum_i \Delta G_i \approx -5.73$ eV, indicating an overbinding of molecular O_2 by approximately 0.81 eV. To this end, we applied a uniform correction of −0.81 eV to the computed O_2 energy, effectively reducing the overbinding and ensuring that the total ORR free-energy cycle sums to −4.92 eV. This corrected O_2 reference was subsequently used for all theoretical overpotential calculations. The correction falls within the range of previously reported values.[6,7]

To maintain consistent surface rumpling amplitude and sinusoidal curvature profiles, a single hydrogen atom was placed near the mountain region in all simulations. The hydrogen atom was positioned away from the M–N_4 center, as shown in Figure S1, for the four curvature values studied. The purpose of this placement was to preserve the curvature pattern across geometries, enabling energetic quantification at positive curvature sites, which are otherwise less stable than negative curvature regions upon adsorption. In the absence of the additional H atom, the curvature magnitudes would become inconsistent. The presence of

this additional H atom does not introduce artificial effects on the local geometry or electronic structure.[8] Since the η^2 geometry at positive curvature (valley) induces larger distortion at the active sites and, during optimization, tends to evolve toward a mountain-like configuration, we performed constrained optimizations to study the curvature-dependent switching between adsorption modes (η^2 and η^1).

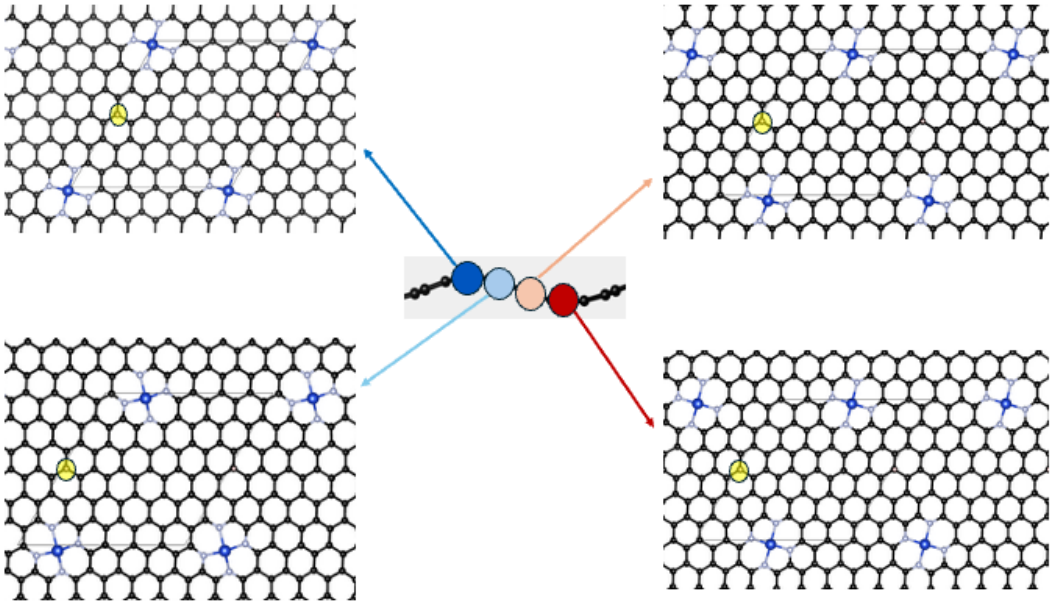

Figure S1: Geometry of the M–N_4 active sites showing the placement of the additional hydrogen atom for the four curvature values studied: –0.13 Å^{-1}, –0.02 Å^{-1}, +0.02 Å^{-1}, and +0.13 Å^{-1}, .

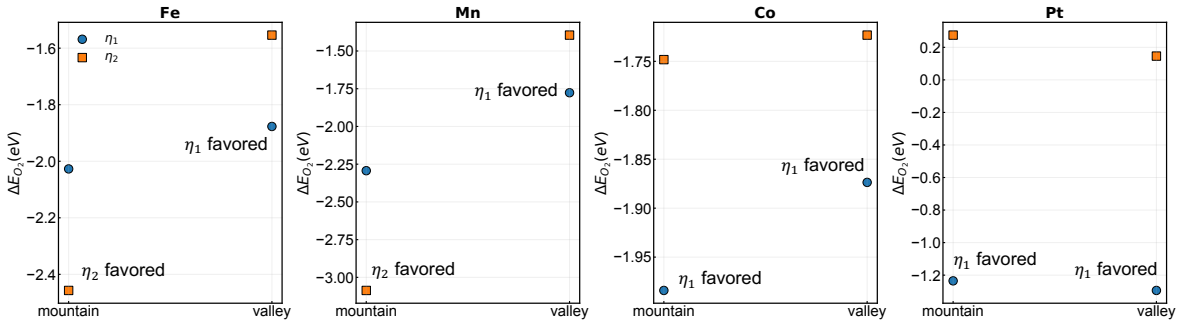

Figure S2: Curvature-dependent preference between η^1 and η^2 O_2 adsorption modes across metals. Adsorption energies, ΔE_{O_2} (eV), are shown for the mountain (-0.12 Å^{-1}) and valley ($+0.12$ Å^{-1}) regions for Fe, Mn, Co, and Pt.

Metal Specific Scaling Relations

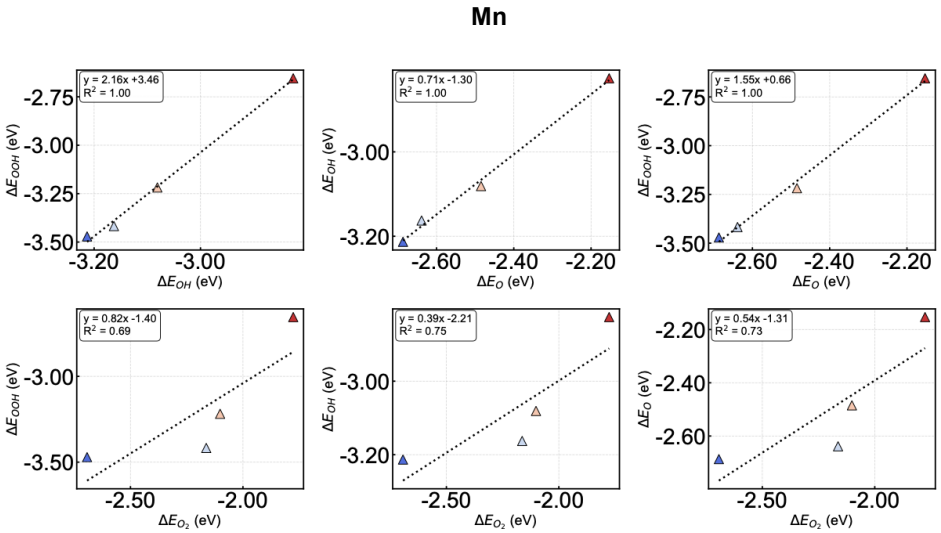

Figure S3: Curvature-dependent binding energies and scaling relations among oxygen reduction reaction (ORR) intermediates (O_2, OOH, O, and OH) for Mn.

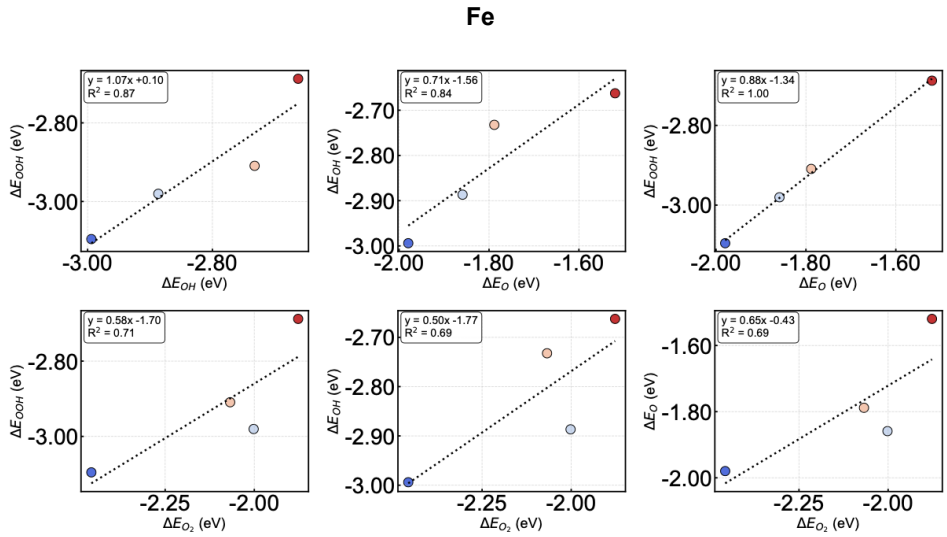

Figure S4: Curvature-dependent binding energies and scaling relations among oxygen reduction reaction (ORR) intermediates (O_2, OOH, O, and OH) for Fe.

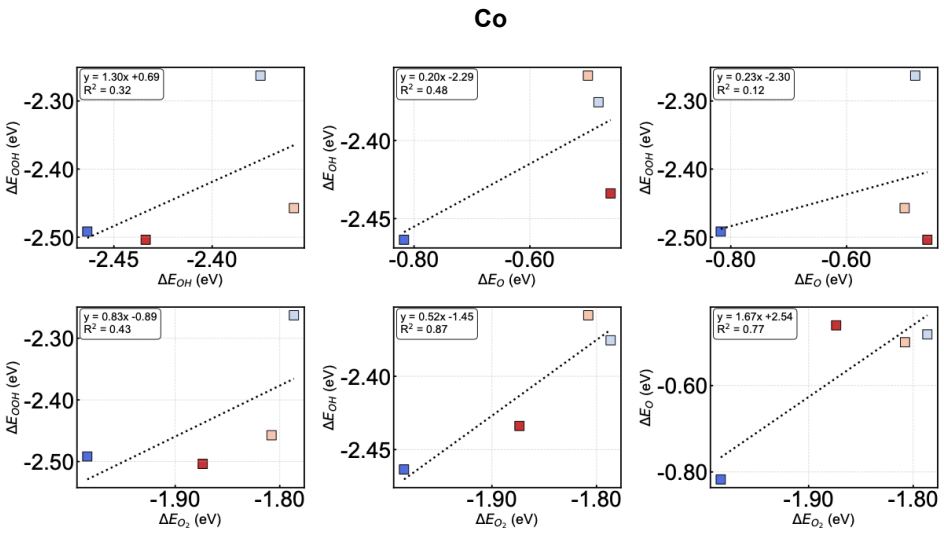

Figure S5: Curvature-dependent binding energies and scaling relations among oxygen reduction reaction (ORR) intermediates (O_2, OOH, O, and OH) for Co.

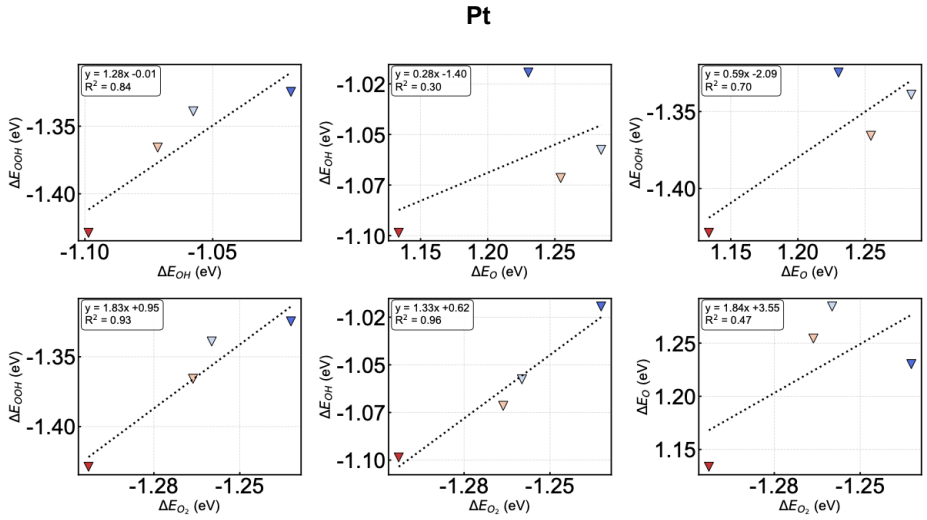

Figure S6: Curvature-dependent binding energies and scaling relations among oxygen reduction reaction (ORR) intermediates (O_2, OOH, O, and OH) for Pt.

Table S1: Per-metal scaling-relation fit parameters ($y = mx + b$) for the six adsorbate-pair regressions.

Metal	Pair (y vs. x)	m (slope)	b (intercept)	R^2
Fe	ΔE_{OOH} vs. ΔE_{OH}	1.07	0.10	0.87
Fe	ΔE_{OH} vs. ΔE_{O}	0.71	−1.56	0.84
Fe	ΔE_{OOH} vs. ΔE_{O}	0.88	−1.34	1.00
Fe	ΔE_{OOH} vs. ΔE_{O_2}	0.58	−1.70	0.71
Fe	ΔE_{OH} vs. ΔE_{O_2}	0.50	−1.77	0.69
Fe	ΔE_{O} vs. ΔE_{O_2}	0.65	−0.43	0.69
Co	ΔE_{OOH} vs. ΔE_{OH}	1.30	0.69	0.32
Co	ΔE_{OH} vs. ΔE_{O}	0.20	−2.29	0.48
Co	ΔE_{OOH} vs. ΔE_{O}	0.23	−2.30	0.12
Co	ΔE_{OOH} vs. ΔE_{O_2}	0.83	−0.89	0.43
Co	ΔE_{OH} vs. ΔE_{O_2}	0.52	−1.45	0.87
Co	ΔE_{O} vs. ΔE_{O_2}	1.67	2.54	0.77
Mn	ΔE_{OOH} vs. ΔE_{OH}	2.16	3.46	1.00
Mn	ΔE_{OH} vs. ΔE_{O}	0.71	−1.30	1.00
Mn	ΔE_{OOH} vs. ΔE_{O}	1.55	0.66	1.00
Mn	ΔE_{OOH} vs. ΔE_{O_2}	0.82	−1.40	0.69
Mn	ΔE_{OH} vs. ΔE_{O_2}	0.39	−2.21	0.75
Mn	ΔE_{O} vs. ΔE_{O_2}	0.54	−1.31	0.73
Pt	ΔE_{OOH} vs. ΔE_{OH}	1.28	−0.01	0.84
Pt	ΔE_{OH} vs. ΔE_{O}	0.28	−1.40	0.30
Pt	ΔE_{OOH} vs. ΔE_{O}	0.59	−2.09	0.70
Pt	ΔE_{OOH} vs. ΔE_{O_2}	1.83	0.95	0.93
Pt	ΔE_{OH} vs. ΔE_{O_2}	1.33	0.62	0.96
Pt	ΔE_{O} vs. ΔE_{O_2}	1.84	3.55	0.47

Electronic Descriptors Derived from PDOS Analysis

To quantify the curvature-dependent electronic structure at the active site, we extracted a set of band-structure and orbital-overlap descriptors from the projected density of states (PDOS) of the metal (d states) and the coordinating oxygen (p states). All energies were aligned with respect to the Fermi level (E_{F}).

Band-center calculation. The metal d-band center (ε_d) and oxygen p-band center (ε_p) were computed as the first moments of their respective PDOS within the valence window:

$$\varepsilon_i = \frac{\displaystyle\int_{E_{\min}}^{E_{\max}} E\, D_i(E)\, dE}{\displaystyle\int_{E_{\min}}^{E_{\max}} D_i(E)\, dE}, \qquad i \in \{d,\, p\}, \tag{1}$$

where $D_i(E)$ denotes the projected density of states for the corresponding orbital manifold. The integration range $[E_{\min}, E_{\max}]$ typically spans from -10 to $+5$ eV relative to E_{F}, encompassing both valence and near-conduction features relevant to adsorption. For the p-band centers, depending on the number and position of O atoms, $\varepsilon_{p,\alpha}$ and $\varepsilon_{p,\beta}$ are calculated.

Normalized overlap integrals. To quantify the degree of orbital hybridization between metal and ligand states, we evaluated the normalized overlap between $D_d(E)$ and $D_p(E)$ as

$$S(E_1, E_2) = \frac{\displaystyle\int_{E_1}^{E_2} D_d(E)\, D_p(E)\, dE}{\sqrt{\displaystyle\int_{E_1}^{E_2} D_d(E)^2\, dE \int_{E_1}^{E_2} D_p(E)^2\, dE}}, \tag{2}$$

which ranges between $0 \leq S \leq 1$.

Orbital-overlap descriptors. From Eq. 2, we define two physically distinct overlap measures:

$$S_{\text{total}} = S(-10,\, 5), \tag{3}$$

$$S_{\text{bonding}} = S(-10,\, 0), \tag{4}$$

corresponding to the total and bonding (occupied) contributions, respectively.

In combination with the band centers ε_d and ε_p, these normalized overlap descriptors provide a physically interpretable representation of curvature-induced electronic-structure variations. The regression models associated with these descriptors are shown in Figs. S2–S3.

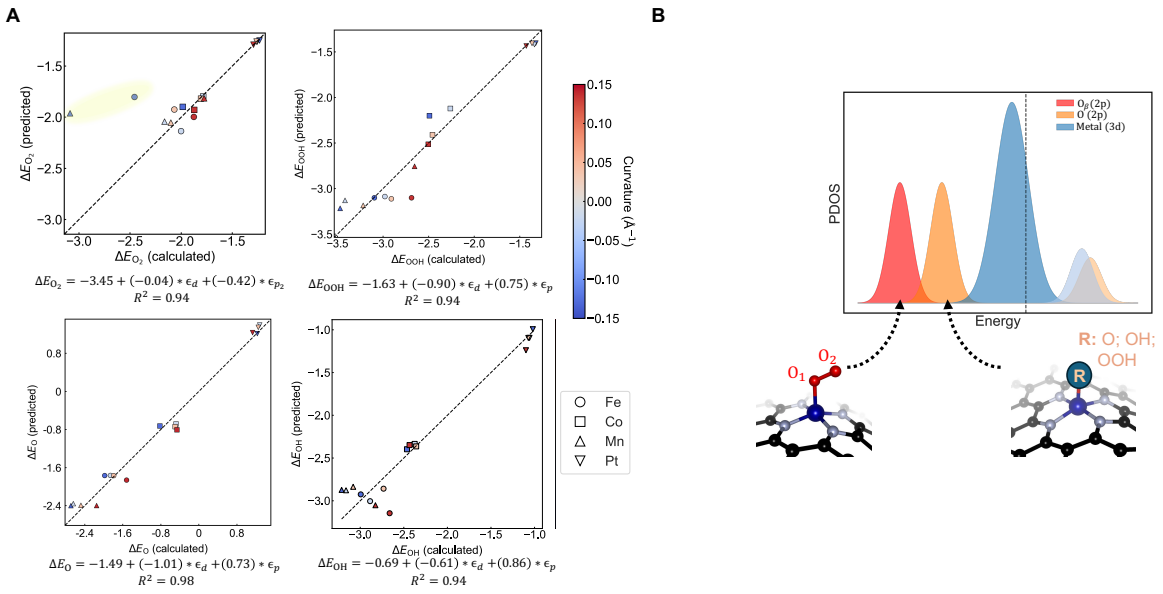

Figure S7: Global linear regression (LR) models based on the metal d-band and oxygen p-band centers capture the binding-energy trends across curvature regions for all four metals. Data points corresponding to η^2 O_2 adsorption are highlighted in yellow. Top-left panel fit excludes the η^2 O_2 points. Although the model R^2s are decent, the fit cannot capture metal-specific trends.

Table S2: Linear regression model details as reported in Figure 4 in the main text.

adsorbate	metal	number of descriptor(s)	descriptor 1	descriptor 2	coefficient_1	coefficient_2	R^2	BE range (eV)
O	Co	1	S_{bonding}		0.14		0.85	0.36
O	Co	2	ε_p	S_{bonding}	−0.07	0.18	1.00	0.36
O	Fe	1	S_{total}		0.17		0.98	0.46
O	Fe	2	ε_d	S_{bonding}	−0.02	0.18	0.98	0.46
O	Mn	1	S_{total}		0.20		0.86	0.54
O	Mn	2	S_{total}	S_{bonding}	0.23	0.07	0.93	0.54
O	Pt	1	ε_d		−0.05		0.65	0.15
O	Pt	2	ε_d	ε_p	−0.08	0.05	0.96	0.15
O_2	Co	1	ε_{p_2}		−0.06		0.62	0.20
O_2	Co	2	ε_d	ε_{p_1}	0.23	−0.26	1.00	0.20
O_2	Fe	1	$S^{p_1}_{\text{total}}$		−0.21		0.92	0.58
O_2	Fe	2	ε_d	ε_{p_2}	0.52	−0.34	1.00	0.58
O_2	Mn	1	ε_{p_1}		−0.47		0.92	1.30
O_2	Mn	2	ε_{p_2}	$S^{p_1}_{\text{bonding}}$	−0.28	−0.48	1.00	1.30
O_2	Pt	1	ε_{p_2}		−0.02		0.95	0.06
O_2	Pt	2	ε_{p_1}	ε_{p_2}	0.06	−0.08	1.00	0.06
OH	Co	1	S_{total}		−0.04		0.86	0.11
OH	Co	2	ε_p	S_{bonding}	−0.04	−0.06	1.00	0.11
OH	Fe	1	ε_p		0.08		0.34	0.33
OH	Fe	2	S_{total}	S_{bonding}	0.25	−0.25	0.99	0.33
OH	Mn	1	ε_p		−0.13		0.78	0.39
OH	Mn	2	S_{total}	S_{bonding}	−0.70	0.59	0.89	0.39
OH	Pt	1	ε_p		0.03		0.81	0.08
OH	Pt	2	ε_d	ε_p	−0.01	0.04	0.93	0.08
OOH	Co	1	S_{bonding}		−0.10		0.94	0.24
OOH	Co	2	S_{total}	S_{bonding}	0.47	−0.56	1.00	0.24
OOH	Fe	1	ε_{p_2}		−0.05		0.13	0.41
OOH	Fe	2	ε_d	ε_{p_2}	0.22	−0.23	0.99	0.41
OOH	Mn	1	S_{bonding}		0.31		0.91	0.82
OOH	Mn	2	ε_d	S_{total}	−0.53	−0.26	1.00	0.82
OOH	Pt	1	ε_d		−0.03		0.73	0.10
OOH	Pt	2	ε_d	ε_{p_1}	−0.15	0.12	0.82	0.10

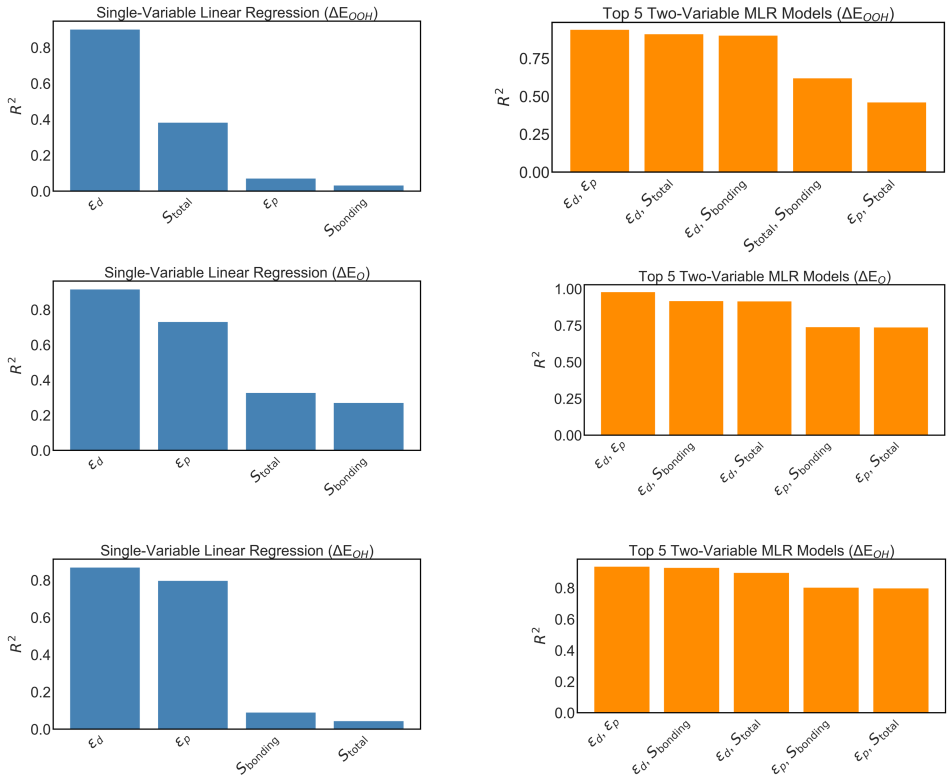

Figure S8: Global regression model details associated with global O, OH, and OOH binding.

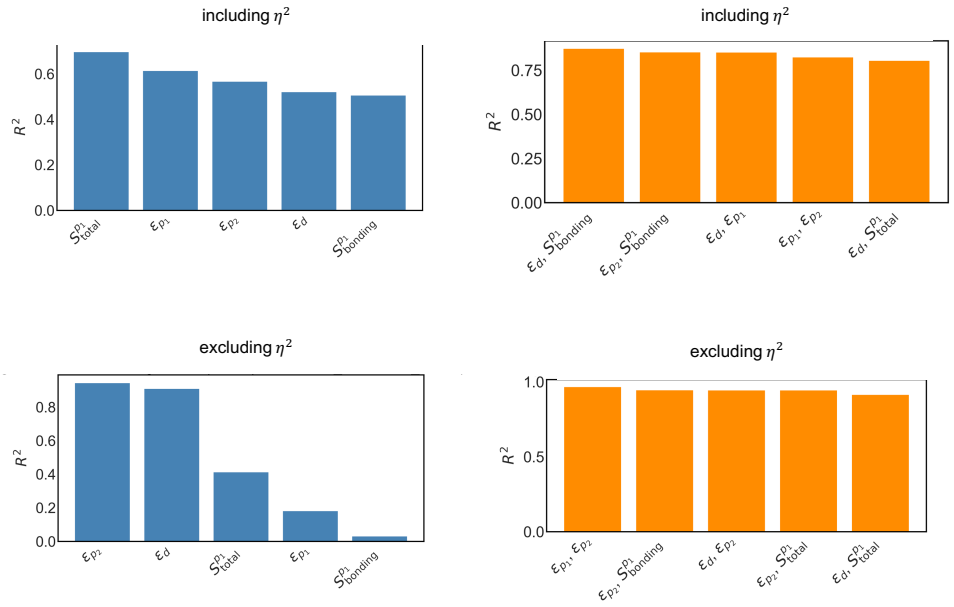

Figure S9: Global regression model details associated with O_2 binding.

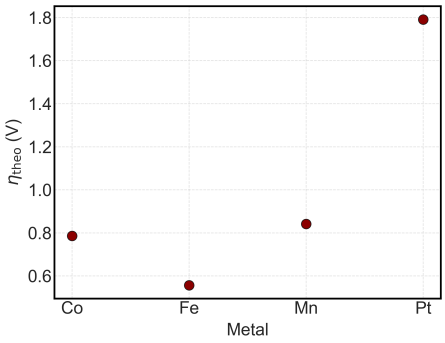

Figure S10: Reported overpotential for the flat configuration.

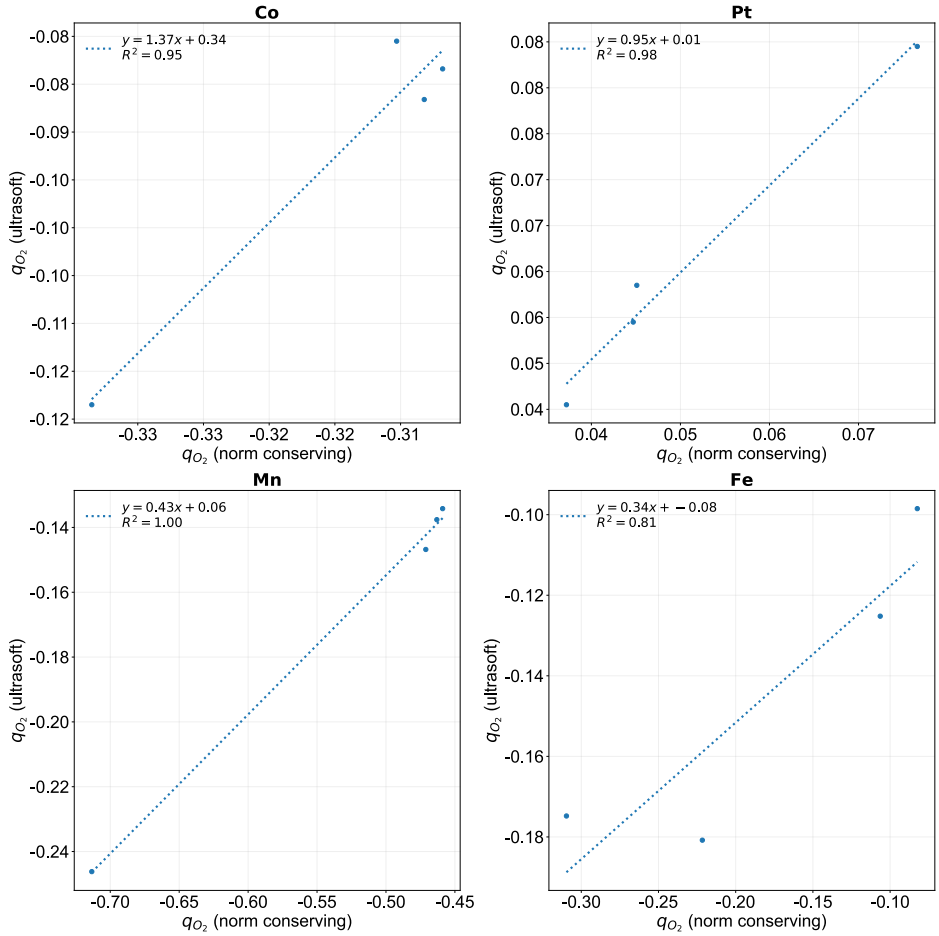

Figure S11: Comparison of Löwdin charges computed using ultrasoft and norm-conserving pseudopotentials. For each metal (Fe, Mn, Co, and Pt), the O_2 charge q_{O_2} obtained with ultrasoft pseudopotentials is plotted against the corresponding value obtained with norm-conserving pseudopotentials,[9–11] with a linear fit shown in each panel.

Free Energy Corrections

For any surface reaction written as $1 \rightarrow 2$, the Gibbs free-energy change is defined as

$$\Delta G \equiv G(2) - G(1) = \Delta E_{\mathrm{DFT}} + \Delta G_{\mathrm{corr}}, \tag{5}$$

where ΔE_{DFT} is the 0 K total energy difference obtained from DFT, and the thermal correction term is given by

$$\Delta G_{\mathrm{corr}} = -T\,\Delta S_{\mathrm{gas}} + \Delta G_{\mathrm{vib}}, \tag{6}$$

where ΔS_{gas} is the entropy change of the gas-phase species and ΔG_{vib} accounts for the vibrational free-energy contributions of the adsorbed species.

Gas-phase entropies were obtained from the NIST database, while vibrational frequencies were taken from the CCCBDB database. For adsorbates, vibrational corrections were computed using the active-site model (M–N_4 plus the adsorbate). For example, in the case of the OOH intermediate, phonon calculations were performed for an eight-atom system. The resulting free-energy corrections were then applied to all systems. For each metal, the free-energy correction was first determined for the flat surface and subsequently used as a reference for the corresponding curved configurations of the same metal. Because the bonding motif remains unchanged across curvature values and such corrections do not affect the relative trends—consistent with previous literature—this approximation is justified and was adopted throughout this work.[12] We note that entropic effects at defect sites—e.g., entropy arising from mechanochemical bending and configurational entropy—are not considered in the present analysis.

Coupling between Variable Curvature

To determine the optimal combination of curvature values contributing cooperatively to the oxygen reduction reaction (ORR), we implemented a curvature-coupled site-assignment

scheme. This procedure identifies the sequence of curvature values that minimizes the limiting potential (U_L) and the corresponding theoretical overpotential (η_{theo}).

Inputs. The analysis requires:

- A set of curvature values $\{\kappa_j\}$ representing the available surface sites (e.g., negative curvature, flat, and positive curvature);
- Free-energy data $\Delta G_i(\kappa_j)$ for each elementary ORR step $i \in \{1, 2, 3, 4\}$ and curvature κ_j;
- The equilibrium potential $U_{\text{eq}} = 1.23$ V.

Procedure. All possible curvature assignments for the four ORR steps are first enumerated as

$$\mathcal{A} = \{(\kappa_1, \kappa_2, \kappa_3, \kappa_4) \mid \kappa_i \in \{\kappa_j\}\}.$$

For each possible assignment $A = (\kappa_1, \kappa_2, \kappa_3, \kappa_4) \in \mathcal{A}$, the free energies for the four elementary ORR steps are evaluated by selecting, for each step i, the value of ΔG_i corresponding to the assigned curvature κ_i:

$$G_i = \Delta G_i(\kappa_i), \qquad i \in \{1, 2, 3, 4\}. \tag{7}$$

The potential-limiting step for a given curvature assignment is defined as

$$U_L(A) = \max(G_1, G_2, G_3, G_4). \tag{8}$$

We compute $\eta_{\text{theo}}(A)$ for all curvature combinations in $\mathcal{A}$ and report the full range of overpotential values obtained. The curvature sequence yielding the lowest η_{theo} corresponds to the most favorable cooperative configuration, while the distribution of η_{theo} values across all assignments provides insight into the sensitivity of ORR energetics to curvature coupling.

References

(1) Giannozzi, P. et al. QUANTUM ESPRESSO: a modular and open-source software project for quantum simulations of materials. *Journal of Physics: Condensed Matter* **2009**, *21*, 395502.

(2) Perdew, J. P.; Burke, K.; Ernzerhof, M. Generalized Gradient Approximation Made Simple. *Physical Review Letters* **1996**, *77*, 3865–3868.

(3) Garrity, K. F.; Bennett, J. W.; Rabe, K. M.; Vanderbilt, D. Pseudopotentials for high-throughput DFT calculations. *Computational Materials Science* **2014**, *81*, 446–452.

(4) Grimme, S.; Antony, J.; Ehrlich, S.; Krieg, H. A consistent and accurateab initioparametrization of density functional dispersion correction (DFT-D) for the 94 elements H-Pu. *The Journal of Chemical Physics* **2010**, *132*.

(5) Monkhorst, H. J.; Pack, J. D. Special points for Brillouin-zone integrations. *Physical Review B* **1976**, *13*, 5188–5192.

(6) Chakraborty, D.; Smitshuysen, T. E. L.; Kakekhani, A.; Jespersen, S. P. F.; Banerjee, S.; Krabbe, A.; Hagen, N.; Silva, H.; Just, J.; Damsgaard, C. D.; Helveg, S.; Rappe, A. M.; Nørskov, J. K.; Chorkendorff, I. Reversible Atomization and Nano-Clustering of Pt as a Strategy for Designing Ultra-Low-Metal-Loading Catalysts. *The Journal of Physical Chemistry C* **2022**, *126*, 16194–16203.

(7) Sargeant, E.; Illas, F.; Rodríguez, P.; Calle-Vallejo, F. Importance of the gas-phase error correction for O2 when using DFT to model the oxygen reduction and evolution reactions. *Journal of Electroanalytical Chemistry* **2021**, *896*, 115178.

(8) Banerjee, S.; Rappe, A. M. Mechanochemical Molecular Migration on Graphene. *Journal of the American Chemical Society* **2022**, *144*, 7181–7188.

(9) Rappe, A. M.; Rabe, K. M.; Kaxiras, E.; Joannopoulos, J. D. Optimized pseudopotentials. *Physical Review B* **1990**, *41*, 1227–1230.

(10) Ramer, N. J.; Rappe, A. M. Designed nonlocal pseudopotentials for enhanced transferability. *Physical Review B* **1999**, *59*, 12471–12478.

(11) OPIUM: Pseudopotential Generation Project. `http://opium.sourceforge.net/`, 2007; Accessed: 2007-08-16.

(12) Kulkarni, A.; Siahrostami, S.; Patel, A.; Nørskov, J. K. Understanding Catalytic Activity Trends in the Oxygen Reduction Reaction. *Chemical Reviews* **2018**, *118*, 2302–2312.